Origin of ferroelectricity in germanium-based inorganic halide perovskites

Lingyao Zhang,[1,*] Chang Liu,[1,2,*,†] Rui Chen,[1,3,‡] Musen Li,[1] Xiaoxuan Ma,[1] Xiangyang Kong,[4] David J. Singh,[5] Gian-Marco Rignanese,[2] and Wei Ren[1,§]

[1]*Physics Department, State Key Laboratory of Advanced Refractories, Material Genome Institute, Shanghai Engineering Research Center for Integrated Circuits and Advanced Display Materials, Institute for Quantum Science and Technology, Shanghai University, Shanghai 200444, China*

[2]*Institute of Condensed Matter and Nanosciences, Université catholique de Louvain, B-1348 Louvain-la-Neuve, Belgium*

[3]*Science and Technology on Reliability Physics and Application of Electronic Component Laboratory, China Electronic Product Reliability and Environmental Testing Research Institute, Guangzhou 511370, China*

[4]*School of Materials Science and Engineering, Shanghai Jiao Tong University, Shanghai 200240, China*

[5]*Department of Physics and Astronomy, University of Missouri, Columbia, Missouri 65211, USA*

(Received 17 August 2024; revised 29 October 2025; accepted 19 December 2025; published 6 February 2026)

Compared to ABO_3 oxide perovskites, intrinsic ferroelectricity is less studied in ABX_3 (X = Cl, Br, I) halide perovskites. Nonetheless, it presents unique opportunities, such as achieving ferroelectric photovoltaics with band gaps suitable for the solar spectrum. In this work, we focus on the $CsGeX_3$ halide perovskites as prototypes for investigating the origin of their ferroelectricity and its relationship with other properties. We find that the presence of stereochemically lone pairs on the perovskite B-site is the primary driving force for ferroelectricity, causing off-center displacements of the Ge ions and enhanced covalency with the halide ligands. This contrasts with the behavior of typical ferroelectric oxide perovskites. Our calculations confirm that halide perovskites are intrinsic modest band gap semiconductors. In particular, $CsGeI_3$ exhibits a very favorable band gap of 1.6 eV for photovoltaic applications. Our findings provide valuable insights into the mechanism underlying high-temperature ferroelectricity in halide perovskites with potential optoelectronic applications.

DOI: 10.1103/ytr2-c1zh

I. INTRODUCTION

Ferroelectrics are materials with switchable spontaneous polarization that have numerous applications in electronic, optoelectronic, and electromechanical devices [1], examples of which include sensors, energy conversion devices, and nonvolatile memories [2]. More recently, ferroelectrics have also emerged as a promising avenue for photovoltaics by utilizing polarization-induced charge separation to enhance photovoltaic performance [3–5], showing significant potential for improving solar energy conversion efficiency [5,6]. However, materials with room-temperature ferroelectricity are mainly oxides and have, therefore, band gaps that are too large for solar-energy applications. While they can be modified to induce below band gap absorption, for example, by alloying [6], practical applications would greatly benefit from the development of intrinsic ferroelectrics with suitable band gaps.

Halide perovskites, ABX_3 (where X represents a halide anion, and A and B are cations), are a potentially promising avenue, since they show inherently smaller band gaps. This stems from the lower electronegativity of halogens below F as compared to O, and the weaker Madelung potentials because of the lower charges of ions in X^--based perovskites as compared to oxides with O^{2-}. In fact, many halide perovskites are excellent solar absorbers, particularly hybrid organic-inorganic ones [7,8]. They display a dielectric behavior, which is very close to that of ferroelectrics and could explain their excellent performance as solar absorbers [9]. However, many challenges remain in elucidating the nature of the polar order, particularly in dynamically disordered systems like $CH_3NH_3PbI_3$ and related materials [10–15]. Their polarization arises from the different geometric orientations of the organic molecules. As such, it typically shows low values and is generally limited to low temperature. Apart from this orientational-order variety, robust ferroelectricity in halide perovskites is quite rare. Therefore, elucidating the mechanisms underlying the appearance of ferroelectricity is highly desirable to guide the search for inorganic halide ferroelectrics.

In this regard, the $CsGeX_3$ (X = Cl, Br, I) family is a class of ferroelectrics [16,17] that has been the subject of intense scrutiny. Zhang and coworkers successfully synthesized nanocrystals of $CsGeX_3$ and confirmed ferroelectricity through piezo-response force microscopy and second-harmonic generation [16]. They ascribed the ferroelectricity to rhombohedral off-centering of the Ge atoms due to stereochemically lone pairs [16]. Chen and coworkers produced high-quality millimeter-sized single crystals of $CsGeI_3$ and measured P-E hysteresis loops to substantiate their bulk ferroelectricity [17]. Christensen *et al.* reported

*These authors contributed equally to this work.
†Contact author: changliu@shu.edu.cn
‡Contact author: cinkfly@hotmail.com
§Contact author: renwei@shu.edu.cn

on $CsGeCl_3$ showing anomalous dielectric constants near the Curie transition temperature [18]. However, a comprehensive understanding of the physical and chemical mechanisms driving ferroelectricity in this context is still lacking. Of particular interest is the interplay between the ferroelectric instability and electronic structure of these compounds, as well as their high ferroelectric Curie temperatures.

The $CsGeX_3$ perovskites undergo a direct transition from the paraelectric cubic $Pm\bar{3}m$ structure to the ferroelectric rhombohedral $R3m$ structure at 455 K for $CsGeCl_3$, 540 K for $CsGeBr_3$, and 577 K for $CsGeI_3$ [19]. This is very different from $BaTiO_3$, $KNbO_3$, and related ferroelectric oxide perovskites, which present a cubic-tetragonal-orthorhombic-rhombohedral transition sequence [20–22], while having the same $R3m$ ground state. In these, the phase transitions are driven by the B-site cation [23], whereas the transition observed in $CsGeX_3$ perovskites might reflect a different bonding. Nonetheless, the ferroelectric phase transition was characterized as of order-disorder type based on diffraction data, similar to $KNbO_3$.

Here, we report on a first-principles study of the ferroelectric and related properties of $CsGeX_3$ perovskites. Consistent with prior work, we find that the ferroelectric instability originates from the presence of stereochemically lone pair electrons associated with Ge^{2+}(II). In fact, this activity is associated with a hybridization of the halogen p orbitals contributing to the valence bands with the unoccupied Ge $4p$ orbitals. Thus, the ferroelectric distortion significantly influences the electronic structure, resulting in an optimal band gap suitable for visible-light absorption. Differences in the ferroelectric behavior from traditional ferroelectric oxide perovskites are discussed in terms of the crystal chemistry.

II. RESULTS AND DISCUSSION

The choice of exchange correlation (XC) functional is crucial when studying ferroelectrics, especially for accurately determining lattice parameters, as ferroelectric properties strongly depend on strain. Here, we test various XC functionals for the cubic and ferroelectric phases of $CsGeX_3$, focusing on structural parameters, ferroelectric polarization, band gaps, Born effective charges (BECs), Bader charges, optical dielectric constants, and the integrated crystal orbital bond index (ICOBI) values, with computational details in the Supplemental Material [24] (see also Refs. [25–58]). Both PBEsol [50] and meta-GGA r^2SCAN [25] functionals are found to accurately describe the structural properties of these materials. The r^2SCAN functional produces results that most closely match experimental data, consistently with findings from previous studies [59]. Furthermore, it predicts higher polarization values than PBEsol owin to larger atomic distortions, aligning better with experimental data. Using r^2SCAN -optimized structures, we calculate the band gaps with different XC functionals including spin-orbit coupling, which is crucial for ferroelectric photovoltaic materials. PBEsol significantly underestimates all the band gaps, while r^2SCAN improves the predictions but still presents a deviation of ∼1 eV. The other two meta-GGA functionals (HLE17 [39,40] and MTASK [28,46]) provide closer estimates, except for the paraelectric phases of $CsGeBr_3$ and $CsGeCl_3$, with ∼0.3 eV difference with respect to the experimental values. The hybrid HSE06 functional typically produces results 0.1–0.3 eV lower than those obtained with the meta-GGA functionals. These findings about the different XC functionals are consistent with what has been observed in a large variety of semiconductors and insulators [60].

The calculated phonon spectra of the cubic perovskites at 0 K are reported in Fig. 1 for $CsGeCl_3$, and in Fig. S1 within the Supplemental Material [24] for (a) $CsGeBr_3$ and (b) $CsGeI_3$. The different phonon modes are colored according to the contributions of Cs (red), Ge (green), and halide (blue) atoms based on the normalized eigenvector of the dynamical matrix, although it should be noted that in general the modes have mixed character. All three materials show strong phonon instabilities in the polar transverse optic (TO) branch at the zone center. This mode shows dominant contributions from Ge and halogen and, beause of the cubic symmetry, it is twofold degenerate. The corresponding longitudinal optic (LO) branch is at high frequency, in the upper part of the phonon dispersions, reflecting a strong LO-TO splitting that is also a well-known characteristic of many ferroelectric oxide perovskites [32,61]. This is a consequence of the large BECs for the materials considered in this work, as reported in Table I. Particularly noteworthy is the very large enhancement of the BEC of Ge in all the compounds. This is a feature that arises from the hybridization between Ge and halogen p states as discussed in previous works for other materials with p electron orbitals and lone pair active ions [62]. The BEC of Ge shows a strong increasing trend as the halogen atom changes from Cl to I. This was expected since the electronegativity of the halogen decreases going down the series, and the band gap correspondingly also decreases, as shown in Table I. These favor an increased hybridization and thus enhance the BEC. Interestingly, the Bader charges, which are a decomposition of the static charge density, do not present any enhancement.

It is worth noting that while ferroelectricity is a relatively common phenomenon in oxide perovskites, it might not be the case in inorganic halide perovskites. In the former, the lattice vibrational modes are softened and the BECs enhanced because of the combination of rather strong Coulomb interactions and the hybridization of cation states, particularly unoccupied cation d states, with the occupied O p states [63]. In the latter, the Coulomb interactions are typically weaker because of the lower valence, resulting in ferroelectricity being uncommon in these materials. However, in the $CsGeX_3$ family under consideration, the weaker Coulomb interactions are apparently compensated by the exceptionally large enhancement of the BECs.

The ferroelectric state arises from the condensation of the unstable TO polar modes. Because of the cubic symmetry, the three Cartesian directions are equivalent, and therefore at the lowest order in the displacement, the instability is isotropic. We calculate the energetics by freezing the soft modes along the [001], [011], and [111] directions. The largest energy gain is along the [111] direction, which is consistent with the observed $R3m$ polar structure. Interestingly, the ground state of the $CsGeX_3$ family has, thus, the same rhombohedral symmetry as the low-temperature structures of $BaTiO_3$ and $KNbO_3$. These oxides show a sequence of phase changes

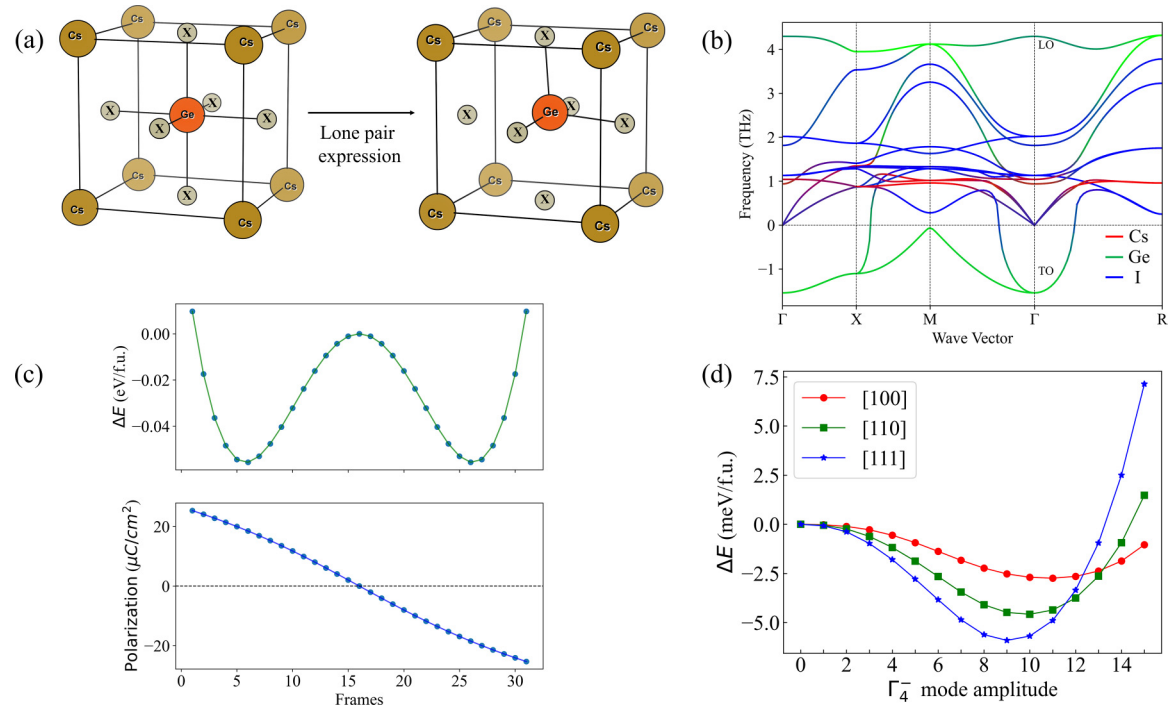

FIG. 1. (a) Structure of the cubic paraelectric and rhombohedral ferroelectric phases of $CsGeX_3$. (b) Phonon dispersion of cubic $CsGeCl_3$. (c) Double-well energy profile and polarization reversal as a function of atomic displacements in ferroelectric phase. (d) Energy profile along three different directions of cubic $CsGeCl_3$ associated with the Γ_4^- soft mode.

TABLE I. Structural parameters, ferroelectric polarization, band gap, Born effective charges (BECs), Bader charges, optical dielectric constant, and integrated crystal orbital bond index (ICOBI) of cubic and ferroelectric phases of $CsGeX_3$ (X = Cl, Br, I).

Compounds Space group		$CsGeCl_3$ $Pm\bar{3}m$	$CsGeCl_3$ $R3m$	$CsGeBr_3$ $Pm\bar{3}m$	$CsGeBr_3$ $R3m$	$CsGeI_3$ $Pm\bar{3}m$	$CsGeI_3$ $R3m$
Lattice constants (Å)	Experiment	5.47[a]	5.43[a]	5.69[a]	5.63[a]	6.05[a]	5.98[a]
	PBEsol	5.21	5.29	5.47	5.49	5.83	5.83
	r^{2}SCAN	5.27	5.43	5.54	5.68	5.94	6.06
Polarization (μC/cm^2)	Experiment				12–15[b]		20[b], 8[c]
	PBEsol		18.46		12.28		12.85
	r^{2}SCAN		24.33		19.24		17.45
Band gap (eV)	Experiment		3.25[b]		2.38[b]		1.60[b,c]
	PBEsol	0.45	1.20	0.36	1.11	0.26	0.78
	r^{2}SCAN	0.66	2.13	0.54	1.40	0.36	0.97
	HLE17	0.91	2.91	1.26	2.09	0.85	1.46
	MTASK	1.02	2.03	0.86	2.01	0.51	1.34
	HSE06	0.99	2.51	0.83	1.70	0.61	1.23
	DSH		3.54[d]		2.68[d]		1.77[d]
Born effective charges (e)	$\boldsymbol{Z}^*_{Cs}$	1.33	1.33	1.33	1.29	1.35	1.29
	$\boldsymbol{Z}^*_{Ge}$	4.97	3.79	5.61	4.96	6.59	5.61
	$\boldsymbol{Z}^*_{X11}$	–4.96	–3.73	–5.45	–4.57	–6.13	–4.90
	$\boldsymbol{Z}^*_{X33}$	–0.67	–0.70	–0.74	–0.84	–0.90	–1.00
Bader charges (e)	$\boldsymbol{Z}_{Cs}$	0.86		0.84		0.82	
	$\boldsymbol{Z}_{Ge}$	0.95		0.98		0.53	
	$\boldsymbol{Z}_{X}$	–0.60		–0.61		–0.45	
Optical dielectric constant ϵ_∞		6.38	4.74	8.00	6.34	10.32	7.92
ICOBI of Ge-X		0.38	0.59	0.39	0.55	0.40	0.53

[a]Reference [19].
[b]Reference [16].
[c]Reference [17].
[d]Reference [64].

(cubic-tetragonal-orthorhombic-rhombohedral) as the temperature decreases. The phase changes are associated with an order-disorder transition in which chain-like correlations arise from TO phonon instabilities in the $\Gamma-X-M$ sheets, but not away from these sheets (i.e., around R for example) [21,22]. This is also a characteristic of the $CsGeX_3$ family, and in fact, diffraction data do suggest a significant order-disorder character. Nonetheless, experiments also show a single direct cubic-rhombohedral ferroelectric transition without other intermediate phases.

We now move to the study of ferroelectric polarization. We use the Berry phase approach to explore the ferroelectric properties of the three compounds. In Fig. 1(c), polarization and energy are reported as functions of the polar atomic distortion. The energy curve corresponds to a double-well potential typical of ferroelectrics. The associated transition barrier is 0.055 eV per formula. This suggests that the polarization could be switched by applying an external electric field. With PBEsol, we find spontaneous polarization values of 18.46 $\mu C/cm^2$, 12.28 $\mu C/cm^2$, and 12.85 $\mu C/cm^2$ for $CsGeCl_3$, $CsGeBr_3$, and $CsGeI_3$, respectively. We note that the choice of the XC functional significantly affects these results due to variations in the atomic positions, as detailed in Table I.

We now turn to the investigation of the origin of ferroelectric instability. While the previous section focused on the analysis of the phase transitions based on the reciprocal space (the phonon dispersion), we here consider the system's structural energetics via the interatomic force constants (IFCs) in real space. By definition, the IFCs $C_{\alpha,\beta}(l\kappa, l'\kappa')$ relate the α component of the force $F_\alpha(l\kappa)$ on atom κ in cell l, to the induced displacement $\tau_\beta(l'\kappa')$ on atom κ' in cell l', according to the expression $F_\alpha(l\kappa) = -C_{\alpha,\beta}(l\kappa, l'\kappa')\tau_\beta(l'\kappa')$ [35]. If the induced force on atom κ is opposite to the displacement direction of atom κ', this leads to discordant cooperative atomic motions, producing a dipole moment. In such a case, the IFCs is positive and corresponds to a destabilizing interaction.

According to Cochran's "soft mode" theory, ferroelectric phase transitions are attributed to q points with unstable TO phonons corresponding to polar atomic distortion modes in the parent paraelectric phase [65,66]. Shell model calculations indicated that this ferroelectric instability results from a competition between stable short-range (SR) forces and unstable dipole long-range (LR) Coulomb interactions, typically in the form of dipole-dipole interactions. Following Cochran's theory, the IFCs can be separated into two contributions [67]: that resulting from the SR forces and that originating from the LR Coulomb (dipole-dipole) interactions; thus, $\frac{\langle\eta|\tilde{D}|\eta\rangle}{\omega^2} = \frac{\langle\eta|\tilde{D}_{\mathrm{LR}}|\eta\rangle}{\omega^2_{\mathrm{LR}}} + \frac{\langle\eta|\tilde{D}_{\mathrm{SR}}|\eta\rangle}{\omega^2_{\mathrm{SR}}}$. In this way, the LR and SR parts of the dynamical matrix $\tilde{D}$, which is connected to the Fourier transform of the matrix of IFCs, can be separated. The specific calculation method for LR's contribution to the IFCs is as follows: $C^{\mathrm{LR}}_{\alpha\beta}(0\kappa, j\kappa') = \sum_{\alpha'\beta'} Z^*_{\kappa,\alpha\alpha'} Z^*_{\kappa',\beta\beta'} (\det\epsilon_\infty)^{-\frac{1}{2}} (\frac{(\epsilon^{-1}_\infty)_{\alpha'\beta'}}{D^3} - 3\frac{\Delta_{\alpha'}\Delta_{\beta'}}{D^5})$, where Z^*_κ and ϵ_∞ represent the Born effective charges and the dielectric constant, respectively. $\Delta_\alpha = \sum_\beta (\epsilon^{-1}_\infty)_{\alpha\beta} d_\beta$, $\mathbf{d} = \mathbf{R}_j + \boldsymbol{\tau}_{\kappa'} - \boldsymbol{\tau}_\kappa$ is the vector relating nuclei, and $D = \sqrt{\Delta \cdot \mathbf{d}}$. The Ewald summation technique is used to evaluate the contribution of this dipole-dipole term to the dynamical matrix. Such calculations can be completed using the ABINIT package.

TABLE II. Γ^-_4 transverse optical frequencies squared and interatomic force constants (IFCs, in $Ha/Bohr^2$) for $CsGeX_3$ (X = Cl, Br, I). The total frequencies squared ω^2 are separated into the short-range (ω^2_{SR}) and long-range (ω^2_{LR}) contributions. Selected IFCs between the Ge-X atomic pairs, where longitudinal (||) refers to the atom displacements parallel to the Ge-X chains.

		$CsGeCl_3$	$CsGeBr_3$	$CsGeI_3$
ω^2 (10^4 cm^{-2})	ω^2_T	–0.93	–0.3	–0.24
	ω^2_{LR}	–14.39	–7.57	–5.27
	ω^2_{SR}	13.46	7.27	5.03
IFCs of Ge-X(||) ($Ha/Bohr^2$)	Total	0.00188	0.00102	0.00082
	LR	0.06506	0.06100	0.06661
	SR	–0.06318	–0.05998	–0.06579

In Table II, we decompose the Γ^-_4 TO mode frequencies squared and the IFCs for $CsGeX_3$ into their short-range and long-range contributions. We observe that $\omega^2_{\mathrm{SR}} > 0$ and $\omega^2_{\mathrm{LR}} < 0$ in all the cubic compounds, with the LR forces dominating to induce a net phonon instability and ferroelectric polarization [33]. As mentioned above, the SR repulsive forces tend to counteract the displacements within the system, favoring the remanence of high symmetry. In contrast, the LR Coulomb forces tend to displace the cations and anions, thereby distorting the high symmetry and facilitating the phase transition. The magnitude of the latter forces is related to the ratio of Z^*_κ and ϵ_∞. In this context, anomalously large BECs, which are significantly greater than their nominal charges, are the primary reason for the strong LR Coulomb forces, such as those found in $CsGeX_3$, particularly for Ge^{2+}. This is related to the covalent bonds between Ge and X halides, which will be explained in detail later. Moreover, we can see that the IFCs for these materials are positive, indicating instability primarily caused by LR dipole-dipole interactions between Ge-X bonds.

In Fig. 2(a), we report the normalized trace of IFC tensors for $CsGeCl_3$ as a function of the atomic distance, which characterizes how the effective interatomic coupling strength varies with atomic separation. To obtain a coordinate-invariant scalar measure of stiffness, we take the tensor trace, $\mathrm{Tr}[C(l\kappa, l'\kappa')] = \sum_\alpha C_{\alpha\alpha}(l\kappa, l'\kappa')$. Then to compare materials with different absolute bond strengths, we normalize it by the on-site self-interaction term, $\tilde{C}(l\kappa, l'\kappa') = \frac{-\mathrm{Tr}[C(l\kappa,l'\kappa')]}{\mathrm{Tr}[C(l\kappa,l\kappa)]}$ [68]. This dimensionless ratio represents the relative intershell coupling strength, which is independent of the overall lattice hardness. Positive normalized traces therefore denote in-phase (antispring) long-range couplings that weaken the restoring force and soften the TO mode, thus promoting polar correlations, whereas negative values correspond to conventional restoring interactions.

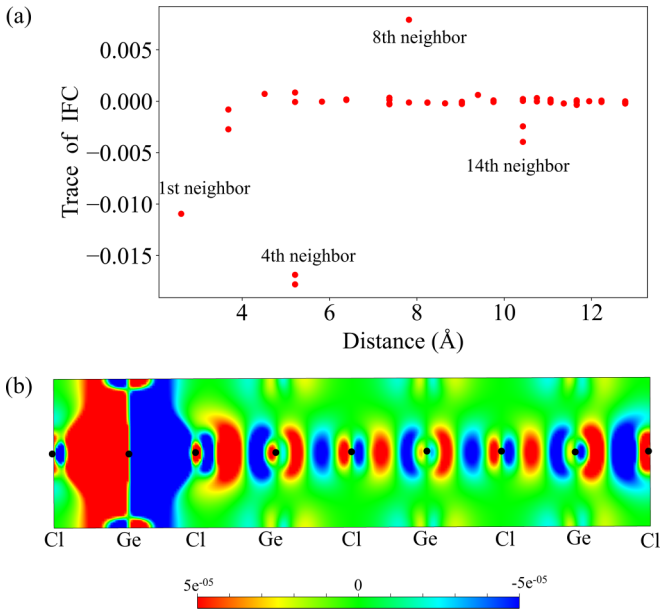

FIG. 2. (a) Normalized trace of the interatomic force constant tensors in $CsGeCl_3$ as a function of the atomic distance. (b) Change in the electron density distribution in the ⟨001⟩ plane because of the displacement of the Ge atom. Each black dot represents an atom.

As shown in Fig. 2(a), the interaction between the fourth-nearest-neighbor at ≈5.2 Å is stronger than that of the first-neighbor Ge–Cl bond at ≈2.6 Å and much stronger than the second- and third-neighbor couplings. The eighth-neighbor at ≈7.8 Å exhibits positive normalized IFCs, indicating the presence of such in-phase (anti-spring) long-range couplings associated with a resonant-bond-driven polarization, while the fourteenth-neighbor beyond 10 Å still maintains a non-negligible interaction. Figure 2(b) illustrates the microscopic origin of these long-range and nonmonotonic IFCs through the charge-density-difference map $\Delta n(\mathbf{r})$, defined as $\Delta n(\mathbf{r}) = n_{\text{displaced}}(\mathbf{r}) - n_{\text{equilibrium}}(\mathbf{r})$, obtained by displacing the Ge^{2+} cation by 0.001 Å along ⟨001⟩.

The resulting $\Delta n(\mathbf{r})$ shows alternating charge polarization that extends up to ≈10 Å along the same direction—well beyond the first coordination shell—demonstrating that the resonant-bond network mediates a long-range electronic response. This real-space polarization pattern directly confirms the IFC analysis in Fig. 2(a): the long-range, in-phase ("anti-spring") couplings, particularly the positive eighth-neighbor term, arise from the displacement-induced polarization of the *p*-electron states of Ge^{2+}. Similar behavior was found in IV–VI resonant-bonded systems, where the highly polarizable *p* electrons of group-IV cations produce comparable long-range charge-density variations [68]. This mechanism resembles that of lone-pair-active ions in classic ferroelectrics, such as $PbTiO_3$, which likewise drive polar distortions through asymmetric p-orbital hybridization.

To demonstrate this point, we also conduct a detailed analysis of the electronic structure and chemical bonding for cubic $CsGeCl_3$. We compute the element-projected band electronic structure (so-called fat band plots), the projected density of states (PDOS), and the projector crystal orbital Hamilton population (-pCOHP), as shown in Figs. 3(a) and 3(b). The analysis of the band structure reveals that $CsGeCl_3$ is a semiconductor characterized by a high dispersion, with a band gap occurring at the *R* point, estimated to be approximately 1 eV (using the HSE06 functional). This band gap is about 0.1 eV and 0.3 eV larger than those of $CsGeBr_3$ and $CsGeI_3$, respectively. From the fat bands and PDOS, we observe that the conduction band minimum is primarily related to the hybridized Ge *p* and Cl *p* orbitals, whereas the valence band is predominantly associated to the Cl *p*, Ge *s*, with a minor contribution from the Ge *p* orbitals. The Cl *p* contributions to the conduction band and the Ge *p* character of the valence bands reflect the hybridization. Note that the main Ge s states are located at lower energies below the main Cl *p* derived valence bands. Therefore, the Ge *s* character appearing in the upper part of the valence band is of antibonding nature. This is confirmed by the -pCOHP analysis. The Cs orbitals (shown in blue) are located further away in energy and are not considered further in our study. Based on the -pCOHP analysis, the valence band states can be divided into three regions: Region I (from –3.9 to 0 eV) corresponding to Ge *s* - Cl *p* antibonding states, Region II (from –6.8 to –3.9 eV) associated with Ge *p* - Cl *p* bonding states, and Region III (from –11 to –6.8 eV) connected with Ge *s* - Cl *p* bonding states. The crystal symmetry is broken by atomic distortions, mixing the Ge and *X* orbitals with empty Ge *p* orbitals. This reduces the antibonding states below the Fermi level and thus lowers the energy through the second-order Jahn-Teller (SOJT) effect [69,70], In this regard, Cl *p* – Ge *p* hybridization is particularly important, as this is a hybridization between a nominally occupied orbital on the anion and a nominally unoccupied orbital on the cation. Hybridization between occupied and unoccupied orbitals is generally the most important type of hybridization for bonding. Furthermore, since these are on different sites, it provides a direct mechanism for enhancing the BECs. It is important to observe that there is a very large increase of the band gap with the ferroelectric distortion, as seen in Table I. This shows the strong interaction between the structure and the electronic structure, as also reflected in the large enhancement of the BECs.

Figures 3(c)–3(g) illustrate the hybridization process in the cubic phase. Region III at the bottom of the valence band consists of a σ bond between Ge *s* and Cl *p*, as also shown in the maximally localized Wannier functions (MLWFs) (e) and (g). Region I at the top of the valence band is associated to an antibonding state σ^* between Ge *s* and Cl *p* electrons. These are localized on the corresponding atoms and present spherical symmetry, with no overlap of the MLWFs (d). This is typical of high-energy antibonding states. Such antibonding states at the top of the valence band are generally regarded as favorable for optoelectronic materials, since they increase band dispersions and thus the carrier mobility [71,72]. Note that both the bonding σ and antibonding σ^* states between Ge *s* and Cl *p* electrons are among the occupied bands. Region II contains σ bonding states from empty Ge *p* and Cl *p*, along with secondary bonds from Region I antibonding state and conduction band Ge *p*, crucial for ferroelectric distortions.

We also evaluate the covalent bond strength by means of the integral ICOHP values. In the cubic phase, the

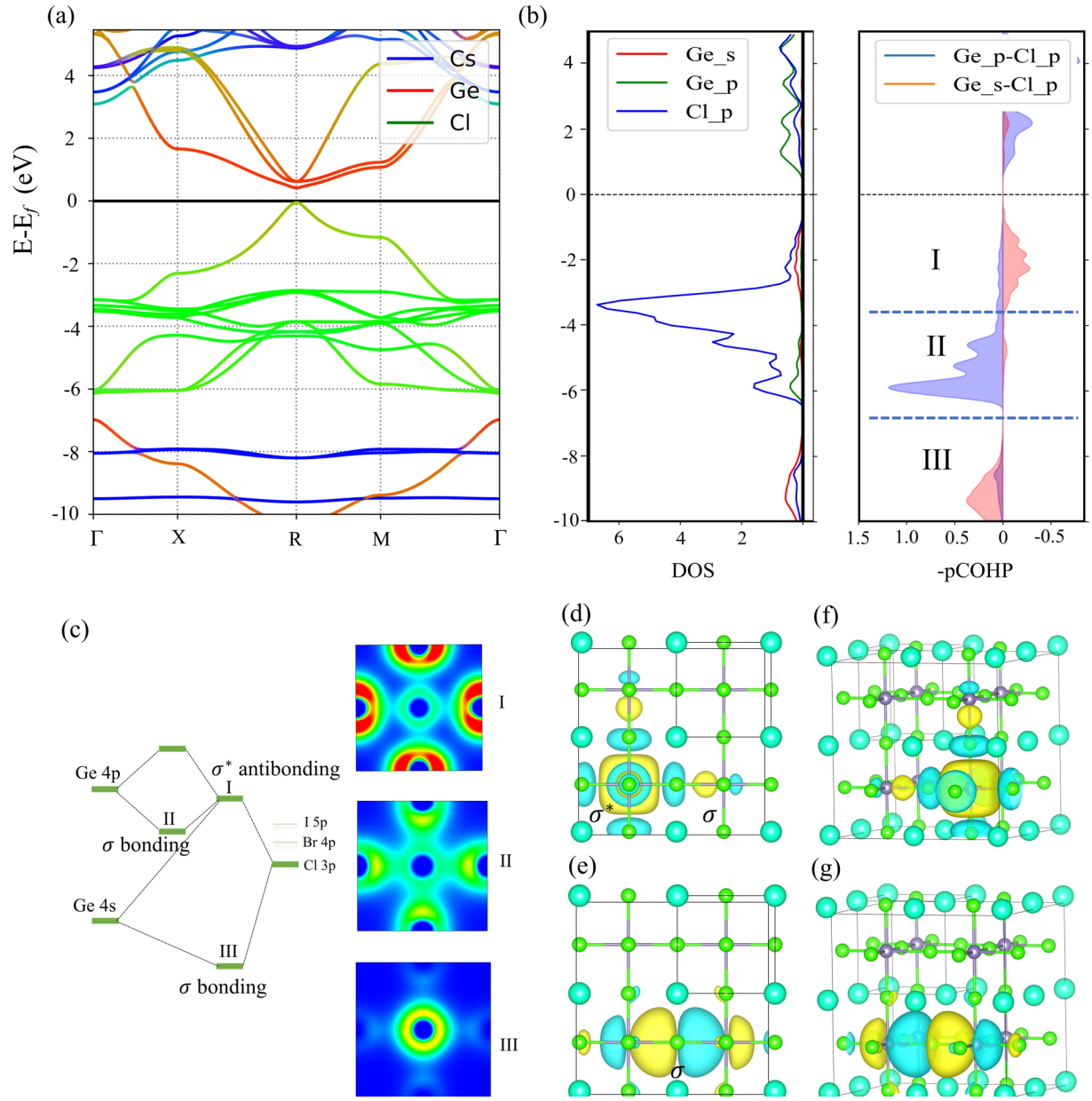

FIG. 3. Electronic structure of cubic paraelectric $CsGeCl_3$. (a) Fat electronic band structure projected onto three different elements (Cs, Ge, Cl). (b) Projected density of states (PDOS) and -pCOHP analysis of the Ge^{2+} atom with nearest neighbors Cl^-. Positive and negative -pCOHPs indicate bonding and antibonding states, respectively. (c) Schematic molecular orbital diagram and corresponding partial charge density of Ge-Cl. (d)–(g) MLWFs illustrating σ bonding (the isosurfaces are illustrated for 1.08×10^{-8} a.u.).

antibonding state (Region I) presents an ICOHP value of –0.4, which decreases to –0.3 in the ferroelectric *R*3*m* structure. This suggests weakened antibonding states and strengthened $p-p$ σ bonds. This is supported by higher ICOBI values and charge population analysis indicating stronger covalent bonding between Ge and halides in the ferroelectric phase. Moreover, the charge population analysis (BECs and Bader charges) reveals σ covalent bonds between Ge and halides, with Z^*_{Ge} and Z^*_{X11} being larger than their nominal charges, hence indicating a partial electron transfer. Finally, we discuss the effect of different halogen ligands on ferroelectric distortions. Substituting Cl with Br and I theoretically should increase ferroelectric instability, but our results show that $CsGeCl_3$ has the highest ICOHP (–0.4), followed by $CsGeBr_3$ (–0.36) and $CsGeI_3$ (–0.31), as shown in Table I. Nonetheless, in spite of the weakening ICOHP going from Cl to I, the ferroelectric instabilities remain strong as seen in the phonon dispersion curves and also in the enhancement of the BECs.

We now briefly turn to crystal chemistry in the $CsGeX_3$ family in relation to ABO_3 oxide perovskites. As already mentioned, high BECs associated with metal-ligand hybridization are important for ferroelectricity in the oxide perovskites. These are also found in the considered halide perovskites. Perovskites are also often characterized by their Goldsmith

perovskite tolerance factor [73] $t = (r_A + r_X)/\sqrt{2}(r_B + r_X)$, where r_A, r_B, and r_X are the ionic radii of the A-site and B-site cations, and of the X anions. Oxide perovskites ($X = O$) that have $t > 1$, such as $KNbO_3$ and $BaTiO_3$, present ferroelectricity. The latter is mostly driven by the displacement of the B-site cation within its O cage. This has been understood in terms of the B-site cation being too small for its site in the ideal cubic lattice. Most oxide perovskites have, however, $t < 1$ and are nonferroelectric. They have structures such as $CaTiO_3$ where the BO_6 octahedra rotate. There are a few exceptions where ferroelectricity does occur even with $t < 1$. These materials display either a stereochemically active A-site ion, such as $BiFeO_3$ and $Pb(Zr,Ti)O_3$, or disorder on the A-site. Those A-site driven ferroelectrics are characterized by off-centering of the A-site cation competing with rotations of the octahedra. In the $CsGeX_3$ family, the A-site is occupied by Cs atoms and the B-site by Ge atoms. Based on the Shannon crystal radii [74], the Goldsmith perovskite tolerance factors are thus 1.027, 1.009, and 0.985 for $CsGeCl_3$, $CsGeBr_3$ and $CsGeI_3$, respectively. Thus, this family spans the full range of possibilities in terms of the t value: from $t > 1$ as in $BaTiO_3$, a classic ferroelectric with a rhombohedral ground state; to t near 1 as in $SrTiO_3$, which approaches ferroelectricity at low temperature, but is not ferroelectric; and $t < 1$ as in $CaTiO_3$, a structure with strong octahedral rotation and no ferroelectricity. In contrast with $BaTiO_3$, $SrTiO_3$, and $CaTiO_3$, the three $CsGeX_3$ compounds are, however, all ferroelectric with similar Curie temperatures and rather similar patterns of unstable modes. There is a relative softening of the lowest phonon branch approaching the R point in $CsGeI_3$, which has $t < 1$ indicating that this material does have a tendency towards rotation of the octahedra compared to the other two materials; however, this is much weaker than, for example, in $CaTiO_3$. Thus, these $CsGeX_3$ ferroelectrics are very different from the oxides in terms of the underlying mechanisms at play. In particular, the $p - p$ hybridization and lone pair physics involving the Ge^{2+} cations and the halogens play a key role, and the ferroelectricity cannot be rationalized simply by ionic radii and tolerance factors.

Our study reveals that stereochemically active $4s^2$ lone pairs and enhanced M–X covalency drive ferroelectric distortion in $CsGeX_3$ [75]. This principle extends to other IVA-group cations (Sn^{2+}, Pb^{2+}) [76,77] and provides a basis for future design strategies. By employing solid solutions, mixed-halide compositions, and chemical pressure through A- or X-site substitution, lattice distortion, band gap, and stability can be systematically tuned. These guidelines offer a concise roadmap for developing next-generation ferroelectric halide perovskites.

III. CONCLUSIONS

In this study, we have investigated the ferroelectric properties and phase transitions of $CsGeX_3$ halide perovskites using density functional theory. Various XC functionals including meta-GGAs were tested and found to provide a very good description of the structural parameters and band gaps. We have conducted a detailed analysis of the phonon dispersion, the ferroelectric polarization, the interatomic force constants, the electronic band structure, and the bonding mechanisms in these halides. The phonon spectra reveal that the polar soft modes, predominantly involving Ge^{2+} and halide ions, are responsible for the onset of ferroelectricity. A significant LO-TO splitting has been observed in all three perovskites because of the large BECs, resulting in a substantial polarization. The stereochemical activity of Ge^{2+} was found to be crucial for ferroelectricity, including p electron hybridization and a SOJT effect. This process breaks the halogen octahedral symmetry. Furthermore, our analysis of real-space IFCs has revealed that the global ferroelectric phase transition is driven by strong long-range interactions between local dipole moments, contributing to its robustness and resulting in high transition temperatures. This study offers critical insights into the ferroelectric and semiconductor properties of $CsGeX_3$, emphasizing their potential for advanced materials applications.

ACKNOWLEDGMENTS

This work was supported by National Natural Science Foundation of China (Grants No. 52130204, No. 12311530675), Science and Technology Commission of Shanghai Municipality (Grant No. 22XD1400900), Shanghai Technical Service Center of Science and Engineering Computing, the supercomputing facilities of UCLouvain (CISM) and Consortium des Equipements de Calcul Intensif en Fédération Wallonie-Bruxelles (CECI). C.L. acknowledges support from the China Scholarship Council, Postdoctoral Fellowship Program of CPSF under Grant No. GZC20252219, Shanghai Super Postdoctoral Incentive Program under Grant No. 2025362. We thank Enrico Marazzi and Victor Trinquet for insightful discussions on the use of ABINIT.

[1] M. E. Lines and A. M. Glass, *Principles and Applications of Ferroelectrics and Related Materials* (Oxford University Press, Oxford, 2001).

[2] J. F. Scott, Applications of modern ferroelectrics, Science **315**, 954 (2007).

[3] V. M. Fridkin, *Photoferroelectrics* (Springer Science & Business Media, Berlin, 2012).

[4] J. Kreisel, M. Alexe, and P. A. Thomas, A photoferroelectric material is more than the sum of its parts, Nat. Mater. **11**, 260 (2012).

[5] S. Y. Yang, J. Seidel, S. J. Byrnes, P. Shafer, C.-H. Yang, M. D. Rossell, P. Yu, Y.-H. Chu, J. F. Scott, J. W. Ager, *et al.*, Above-bandgap voltages from ferroelectric photovoltaic devices, Nat. Nanotech. **5**, 143 (2010).

[6] I. Grinberg, D. V. West, M. Torres, G. Gou, D. M. Stein, L. Wu, G. Chen, E. M. Gallo, A. R. Akbashev, P. K. Davies, *et al.*, Perovskite oxides for visible-light-absorbing ferroelectric and photovoltaic materials, Nature (London) **503**, 509 (2013).

[7] S. D. Stranks, G. E. Eperon, G. Grancini, C. Menelaou, M. J. P. Alcocer, T. Leijtens, L. M. Herz, A. Petrozza, and H. J.

Snaith, Electron-hole diffusion lengths exceeding 1 micrometer in an organometal trihalide perovskite absorber, Science **342**, 341 (2013).

[8] M. A. Green, A. Ho-Baillie, and H. J. Snaith, The emergence of perovskite solar cells, Nat. Photon. **8**, 506 (2014).

[9] M.-H. Du, Efficient carrier transport in halide perovskites: Theoretical perspectives, J. Mater. Chem. A **2**, 9091 (2014).

[10] L. Li, X. Liu, C. He, S. Wang, C. Ji, X. Zhang, Z. Sun, S. Zhao, M. Hong, and J. Luo, A potential Sn-based hybrid perovskite ferroelectric semiconductor, J. Am. Chem. Soc. **142**, 1159 (2020).

[11] Y.-M. You, W.-Q. Liao, D. Zhao, H.-Y. Ye, Y. Zhang, Q. Zhou, X. Niu, J. Wang, P.-F. Li, D.-W. Fu, *et al.*, An organic-inorganic perovskite ferroelectric with large piezoelectric response, Science **357**, 306 (2017).

[12] Y. Liu, L. Collins, R. Proksch, S. Kim, B. R. Watson, B. Doughty, T. R. Calhoun, M. Ahmadi, A. V. Ievlev, S. Jesse, *et al.*, Chemical nature of ferroelastic twin domains in $CH_3NH_3PbI_3$ perovskite, Nat. Mater. **17**, 1013 (2018).

[13] W. Zheng, X. Wang, X. Zhang, B. Chen, H. Suo, Z. Xing, Y. Wang, H.-L. Wei, J. Chen, Y. Guo, *et al.*, Emerging halide perovskite ferroelectrics, Adv. Mater. **35**, 2205410 (2023).

[14] A. Gómez, Q. Wang, A. R. Goñi, M. Campoy-Quiles, and A. Abate, Ferroelectricity-free lead halide perovskites, Energy Environ. Sci. **12**, 2537 (2019).

[15] A. D. Schulz, H. Röhm, T. Leonhard, S. Wagner, M. J. Hoffmann, and A. Colsmann, On the ferroelectricity of $CH_3NH_3PbI_3$ perovskites, Nat. Mater. **18**, 1050 (2019).

[16] Y. Zhang, E. Parsonnet, A. Fernandez, S. M. Griffin, H. Huyan, C.-K. Lin, T. Lei, J. Jin, E. S. Barnard, A. Raja, *et al.*, Ferroelectricity in a semiconducting all-inorganic halide perovskite, Sci. Adv. **8**, eabj5881 (2022).

[17] R. Chen, C. Liu, Y. Chen, C. Ye, S. Chen, J. Cheng, S. Cao, S. Wang, A. Cui, Z. Hu, *et al.*, Ferroelectric $CsGeI_3$ single crystals with a perovskite structure grown from aqueous solution, J. Phys. Chem. C **127**, 635 (2023).

[18] A. N. Christensen, S. E. Rasmussen, P. Karvonen, A. Kjær, R. H. Shapiro, and A. Westerdahl, A ferroelectric chloride of perowskite type crystal structure of $CsGeCl_3$, Acta Chem. Scand. **19**, 421 (1965).

[19] G. Thiele, H. W. Rotter, and K. D. Schmidt, Kristallstrukturen und Phasentransformationen von Caesiumtrihalogenogermanaten(II) $CsGeX_3$ (X = Cl, Br, I), Z. Anorg. Allg. Chem. **545**, 148 (1987).

[20] S. Tinte, M. Sepliarsky, M. G. Stachiotti, R. L. Migoni, and C. O. Rodriguez, Modelling of the phase transitions sequence in $KNbO_3$ and $BaTiO_3$, Z. Phys. B: Condens. Matter **104**, 721 (1997).

[21] M. Lambert and R. Comes, The chain structure and phase transition of $BaTiO_3$ and $KNbO_3$, Solid State Commun. **7**, 305 (1969).

[22] R. Yu and H. Krakauer, First-principles determination of chain-structure instability in $KNbO_3$, Phys. Rev. Lett. **74**, 4067 (1995).

[23] M. Ghita, M. Fornari, D. J. Singh, and S. V. Halilov, Interplay between A -Site and B -Site driven instabilities in perovskites, Phys. Rev. B **72**, 054114 (2005).

[24] See Supplemental Material at http://link.aps.org/supplemental/10.1103/ytr2-c1zh for details on (i) Computational Method, (ii) Phonon Dispersions, and (iii) Band Structures of Ferroelectric Phases.

[25] J. W. Furness, A. D. Kaplan, J. Ning, J. P. Perdew, and J. Sun, Accurate and numerically efficient r^2SCAN meta-generalized gradient approximation, J. Phys. Chem. Lett. **11**, 8208 (2020).

[26] D. Orobengoa, C. Capillas, M. I. Aroyo, and J. M. Perez-Mato, AMPLIMODES: Symmetry-mode analysis on the Bilbao Crystallographic Server, J. Appl. Cryst. **42**, 820 (2009).

[27] J. P. Perdew, J. A. Chevary, S. H. Vosko, K. A. Jackson, M. R. Pederson, D. J. Singh, and C. Fiolhais, Atoms, molecules, solids, and surfaces: Applications of the generalized gradient approximation for exchange and correlation, Phys. Rev. B **46**, 6671 (1992).

[28] F. Tran, J. Doumont, L. Kalantari, P. Blaha, T. Rauch, P. Borlido, S. Botti, M. A. L. Marques, A. Patra, S. Jana, *et al.*, Bandgap of two-dimensional materials: Thorough assessment of modern exchange–correlation functionals, J. Chem. Phys. **155**, 104103 (2021).

[29] P. C. Müller, C. Ertural, J. Hempelmann, and R. Dronskowski, Crystal orbital bond index: Covalent bond orders in solids, J. Phys. Chem. C **125**, 7959 (2021).

[30] V. L. Deringer, A. L. Tchougréeff, and R. Dronskowski, Crystal orbital hamilton population (COHP) analysis as projected from plane-wave basis sets, J. Phys. Chem. A **115**, 5461 (2011).

[31] R. Dronskowski and P. E. Bloechl, Crystal orbital hamilton populations (COHP): Energy-resolved visualization of chemical bonding in solids based on density-functional calculations, J. Phys. Chem. **97**, 8617 (1993).

[32] M. I. Aroyo, J. M. Perez-Mato, D. Orobengoa, E. Tasci, G. de la Flor, and A. Kirov, Crystallography online: Bilbao crystallographic server, Bulg. Chem. Commun. **43**, 183 (2011).

[33] X. Gonze and C. Lee, Dynamical matrices, born effective charges, dielectric permittivity tensors, and interatomic force constants from density-functional perturbation theory, Phys. Rev. B **55**, 10355 (1997).

[34] G. Kresse and J. Furthmüller, Efficiency of *ab-initio* total energy calculations for metals and semiconductors using a plane-wave basis set, Comput. Mater. Sci. **6**, 15 (1996).

[35] G. Kresse and J. Furthmüller, Efficient iterative schemes for *ab initio* total-energy calculations using a plane-wave basis set, Phys. Rev. B **54**, 11169 (1996).

[36] A. Togo, First-principles phonon calculations with phonopy and phono3py, J. Phys. Soc. Jpn. **92**, 012001 (2023).

[37] G. Kresse and D. Joubert, From ultrasoft pseudopotentials to the projector augmented-wave method, Phys. Rev. B **59**, 1758 (1999).

[38] F. Jollet, M. Torrent, and N. Holzwarth, Generation of projector augmented-wave atomic data: A 71 element validated table in the XML format, Comput. Phys. Commun. **185**, 1246 (2014).

[39] I. Choudhuri and D. G. Truhlar, HLE17: An efficient way to predict band gaps of complex materials, J. Phys. Chem. C **123**, 17416 (2019).

[40] P. Verma and D. G. Truhlar, HLE17: An improved local exchange–correlation functional for computing semiconductor band gaps and molecular excitation energies, J. Phys. Chem. C **121**, 7144 (2017).

[41] A. Togo, L. Chaput, T. Tadano, and I. Tanaka, Implementation strategies in phonopy and phono3py, J. Phys.: Condens. Matter **35**, 353001 (2023).

[42] A. V. Krukau, O. A. Vydrov, A. F. Izmaylov, and G. E. Scuseria, Influence of the exchange screening parameter on the performance of screened hybrid functionals, J. Chem. Phys. **125**, 224106 (2006).

[43] Y. Zhang, W. Zhang, and D. J. Singh, Localization in the SCAN meta-generalized gradient approximation functional leading to broken symmetry ground states for graphene and benzene, Phys. Chem. Chem. Phys. **22**, 19585 (2020).

[44] N. Marzari, A. A. Mostofi, J. R. Yates, I. Souza, and D. Vanderbilt, Maximally localized Wannier functions: Theory and applications, Rev. Mod. Phys. **84**, 1419 (2012).

[45] J. M. Perez-Mato, D. Orobengoa, and M. I. Aroyo, Mode crystallography of distorted structures, Acta Cryst. A **66**, 558 (2010).

[46] B. Neupane, H. Tang, N. K. Nepal, S. Adhikari, and A. Ruzsinszky, Opening band gaps of low-dimensional materials at the meta-GGA level of density functional approximations, Phys. Rev. Mater. **5**, 063803 (2021).

[47] P. Bonfà, S. Sharma, and J. K. Dewhurst, Partially deorbitalized meta-GGA, Comput. Mater. Today **1**, 100002 (2024).

[48] F. Tran, R. Laskowski, P. Blaha, and K. Schwarz, Performance on molecules, surfaces, and solids of the Wu-Cohen GGA exchange-correlation energy functional, Phys. Rev. B **75**, 115131 (2007).

[49] S. P. Ong, W. D. Richards, A. Jain, G. Hautier, M. Kocher, S. Cholia, D. Gunter, V. L. Chevrier, K. A. Persson, and G. Ceder, Python materials genomics (pymatgen): A robust, open-source python library for materials analysis, Comput. Mater. Sci. **68**, 314 (2013).

[50] J. P. Perdew, A. Ruzsinszky, G. I. Csonka, O. A. Vydrov, G. E. Scuseria, L. A. Constantin, X. Zhou, and K. Burke, Restoring the density-gradient expansion for exchange in solids and surfaces, Phys. Rev. Lett. **100**, 136406 (2008).

[51] J. Sun, A. Ruzsinszky, and J. P. Perdew, Strongly constrained and appropriately normed semilocal density functional, Phys. Rev. Lett. **115**, 036402 (2015).

[52] C. Capillas, E. Kroumova, M. I. Aroyo, J. M. Perez-Mato, H. T. Stokes, and D. M. Hatch, SYMMODES: A software package for group-theoretical analysis of structural phase transitions, J. Appl. Cryst. **36**, 953 (2003).

[53] X. Gonze, B. Amadon, G. Antonius, F. Arnardi, L. Baguet, J.-M. Beuken, J. Bieder, F. Bottin, J. Bouchet, E. Bousquet, *et al.*, The Abinit project: Impact, environment and recent developments, Comput. Phys. Commun. **248**, 107042 (2020).

[54] M. J. van Setten, M. Giantomassi, E. Bousquet, M. J. Verstraete, D. R. Hamann, X. Gonze, and G.-M. Rignanese, The Pseudodojo: Training and grading a 85 element optimized norm-conserving pseudopotential table, Comput. Phys. Commun. **226**, 39 (2018).

[55] R. D. King-Smith and D. Vanderbilt, Theory of polarization of crystalline solids, Phys. Rev. B **47**, 1651 (1993).

[56] V. Wang, N. Xu, J.-C. Liu, G. Tang, and W.-T. Geng, VASPKIT: A user-friendly interface facilitating high-throughput computing and analysis using VASP code, Comput. Phys. Commun. **267**, 108033 (2021).

[57] G. Pizzi, V. Vitale, R. Arita, S. Blügel, F. Freimuth, G. Géranton, M. Gibertini, D. Gresch, C. Johnson, T. Koretsune, *et al.*, Wannier90 as a community code: New features and applications, J. Phys.: Condens. Matter **32**, 165902 (2020).

[58] A. H. Romero, D. C. Allan, B. Amadon, G. Antonius, T. Applencourt, L. Baguet, J. Bieder, F. Bottin, J. Bouchet, E. Bousquet, *et al.*, ABINIT: Overview and focus on selected capabilities, J. Chem. Phys. **152**, 124102 (2020).

[59] Y. Zhang, J. Sun, J. P. Perdew, and X. Wu, Comparative first-principles studies of prototypical ferroelectric materials by LDA, GGA, and SCAN meta-GGA, Phys. Rev. B **96**, 035143 (2017).

[60] P. Borlido, J. Schmidt, A. W. Huran, F. Tran, M. A. L. Marques, and S. Botti, Exchange-correlation functionals for band gaps of solids: Benchmark, reparametrization and machine learning, npj Comput. Mater. **6**, 1 (2020).

[61] W. Zhong, R. D. King-Smith, and D. Vanderbilt, Giant LO-TO splittings in perovskite ferroelectrics, Phys. Rev. Lett. **72**, 3618 (1994).

[62] X. He, D. J. Singh, P. Boon-on, M.-W. Lee, and L. Zhang, Dielectric behavior as a screen in rational searches for electronic materials: Metal pnictide sulfosalts, J. Am. Chem. Soc. **140**, 18058 (2018).

[63] R. E. Cohen, Origin of ferroelectricity in perovskite oxides, Nature (London) **358**, 136 (1992).

[64] H. Wang, A. Tal, T. Bischoff, P. Gono, and A. Pasquarello, Accurate and efficient band-gap predictions for metal halide perovskites at finite temperature, npj Comput. Mater. **8**, 237 (2022).

[65] W. Cochran, Crystal stability and the theory of ferroelectricity, Phys. Rev. Lett. **3**, 412 (1959).

[66] W. Cochran, Crystal stability and the theory of ferroelectricity, Adv. Phys. **9**, 387 (1960).

[67] P. Ghosez, X. Gonze, and J.-P. Michenaud, Coulomb interaction and ferroelectric instability of $BaTiO_3$, Europhys. Lett. **33**, 713 (1996).

[68] S. Lee, K. Esfarjani, T. Luo, J. Zhou, Z. Tian, and G. Chen, Resonant bonding leads to low lattice thermal conductivity, Nat. Commun. **5**, 3525 (2014).

[69] I. B. Bersuker, On the origin of ferroelectricity in perovskite-type crystals, Phys. Lett. **20**, 589 (1966).

[70] A. Walsh, D. J. Payne, R. G. Egdell, and G. W. Watson, Stereochemistry of post-transition metal oxides: Revision of the classical lone pair model, Chem. Soc. Rev. **40**, 4455 (2011).

[71] S.-C. Liu, C.-M. Dai, Y. Min, Y. Hou, A. H. Proppe, Y. Zhou, C. Chen, S. Chen, J. Tang, and D.-J. Xue, An antibonding valence band maximum enables defect-tolerant and stable GeSe photovoltaics, Nat. Commun. **12**, 670 (2021).

[72] J. S. Manser, J. A. Christians, and P. V. Kamat, Intriguing optoelectronic properties of metal halide perovskites, Chem. Rev. **116**, 12956 (2016).

[73] V. M. Goldschmidt, Die gesetze der krystallochemie, Naturwissenschaften **14**, 477 (1926).

[74] R. D. Shannon, Revised effective ionic radii and systematic studies of interatomic distances in halides and chalcogenides, Acta Cryst. A **32**, 751 (1976).

[75] C. C. Stoumpos, L. Frazer, D. J. Clark, Y. S. Kim, S. H. Rhim, A. J. Freeman, J. B. Ketterson, J. I. Jang, and M. G. Kanatzidis, Hybrid germanium iodide perovskite semiconductors: Active

lone pairs, structural distortions, direct and indirect energy gaps, and strong nonlinear optical properties, J. Am. Chem. Soc. **137**, 6804 (2015).

[76] D. H. Fabini, K. Honasoge, A. Cohen, S. Bette, K. M. McCall, C. C. Stoumpos, S. Klenner, M. Zipkat, L. P. Hoang, J. Nuss, *et al.*, Noncollinear electric dipoles in a polar chiral phase of $CsSnBr_3$ perovskite, J. Am. Chem. Soc. **146**, 15701 (2024).

[77] E. H. Smith, N. A. Benedek, and C. J. Fennie, Interplay of octahedral rotations and lone pair ferroelectricity in $CsPbF_3$, Inorg. Chem. **54**, 8536 (2015).